

Light Element Chemistry and the Double Red Giant Branch in the Galactic Globular Cluster NGC 288

Tiffany Hsyu¹, Christian I. Johnson^{2,4}, Young-Wook Lee³, and R. Michael Rich¹

ABSTRACT

The globular cluster NGC 288 was previously reported to exhibit two distinct red giant branches (RGBs) in the narrow-band Calcium (HK) and Strömgren b and y band passes. In order to investigate this phenomenon further, we obtained moderate resolution ($R \sim 18,000$) spectra of 27 RGB stars in NGC 288 with the Hydra multifiber spectrograph on the Blanco 4m telescope at Cerro Tololo Inter-American Observatory. From these data we derive iron ($\langle[\text{Fe}/\text{H}]\rangle = -1.19$; $\sigma = 0.12$), oxygen ($\langle[\text{O}/\text{Fe}]\rangle = +0.25$; $\sigma = 0.13$), and sodium ($\langle[\text{Na}/\text{Fe}]\rangle = +0.15$; $\sigma = 0.26$) abundances using standard equivalent width and spectrum synthesis techniques. Combining these data with those available in the literature indicates that the two giant branches have distinctly different light element chemistry but do not exhibit a significant spread in $[\text{Fe}/\text{H}]$. A new transmission tracing for the CTIO Ca filter, obtained for this project, shows that CN contamination is the primary spectral feature driving the split RGB. Interestingly, the CN leak in the current CTIO Ca filter may be used as an efficient means to search for CN-weak and CN-strong stars in systems with otherwise small Ca abundance variations.

Subject headings: stars: abundances, globular clusters: general, globular clusters: individual (NGC 288)

1. INTRODUCTION

It has long been known that significant variations in light element abundances exist within almost all globular clusters, and in fact may be a defining characteristic that separates

¹Department of Physics and Astronomy, UCLA, 430 Portola Plaza, Box 951547, Los Angeles, CA 90095-1547, USA; tiffanyhsyu@ucla.edu; rmr@astro.ucla.edu

²Harvard-Smithsonian Center for Astrophysics, 60 Garden Street, MS-15, Cambridge, MA 02138, USA; cjohnson@cfa.harvard.edu

³Center for Galaxy Evolution Research and Department of Astronomy, Yonsei University, Seoul 120-749, Korea; ywlee2@yonsei.ac.kr

⁴Clay Fellow

globular clusters from other stellar populations (e.g., see reviews by Gratton et al. 2004; 2012 and references therein). Recently, these light element variations have been linked to multiple photometric sequences identified by the careful selection of color indices that exploit differences in spectral features between stars, based on their composition (e.g., Monelli et al. 2013; Piotto et al. 2013; see also reviews by Piotto et al. 2009; Gratton et al. 2012). In particular, this has led to the discovery that most globular clusters experienced at least two distinct star formation events. In this scenario, a first generation of stars forms from gas primarily polluted by core-collapse supernovae (SNe) and with a composition nearly identical to metal-poor halo field stars. Subsequently, before all of the gas is lost from the proto-cluster, a second generation forms near the cluster center with the same $[\text{Fe}/\text{H}]$ abundance but exhibiting significantly different light element (e.g., O-poor and Na-rich) chemistry (e.g., D’Ercole et al. 2008; Valcarce & Catelan 2011). The pollution source and formation time scale for the second generation stars are not presently well-constrained, but the leading candidates include intermediate mass asymptotic giant branch (AGB) (e.g., Ventura & D’Antona, 2008; Karakas 2010), rapidly rotating massive main-sequence stars (e.g., Decressin et al. 2007), massive binary stars (e.g., de Mink et al. 2009; Izzard et al. 2013), and possibly super-massive stars (e.g., Denissenkov & Hartwick 2014).

While the small (<0.1 dex) $[\text{Fe}/\text{H}]$ and $[\alpha/\text{Fe}]$ dispersion and typically (inferred) moderate He abundance difference between first and second generation stars in most globular clusters seems to exclude SNe as a significant contributor to the gas from which second generation stars form, Roh et al. (2011) found photometric evidence that NGC 288 stars may exhibit a non-negligible spread in metallicity. The possible metallicity spread is evidenced by a split red giant branch (RGB), observed in the y versus hk^1 color-magnitude diagram, that may be best fit by isochrones in which second generation stars are ~ 1.5 Gyr younger, He-enhanced ($\Delta Y \approx 0.03$), and more metal-rich ($\Delta [\text{M}/\text{H}] \sim 0.16$ dex) than the first generation stars. The observed split RGB in NGC 288 when using the hk index follows similar observations by Lee et al. (2009) of other Galactic globular clusters, and suggests there may be a link between SNe and the well-established light-element variations mentioned previously. However, Carretta et al. (2010) investigated possible $[\text{Ca}/\text{H}]$ variations via spectroscopy in a sample of 200 RGB stars in 17 globular clusters, including NGC 288, and did not find any significant correlations between $[\text{Ca}/\text{H}]$ and light-element chemistry. Consequently, there is a disconnect between the observed spread in RGB sequences produced by the hk index photometry and direct abundance measurements from high-resolution spectroscopy.

In this paper we use high-resolution spectroscopy of RGB stars in NGC 288 to test

¹The hk index is defined in Roh et al. (2011) as $hk = [(Ca-b) - (b-y)]$, where Ca , b , and y are the CTIO Ca and Strömgren b and y filters.

whether any [Fe/H] or light element chemistry differences exist between stars on the two giant branches. We also provide a new transmission curve for the CTIO Ca narrow-band filter, discovering that the apparent population dispersion of NGC 288 was caused by the filter bandpass covering the CN band near 3885 Å and is not due to a dispersion in metallicity.

2. OBSERVATIONS, TARGET SELECTION, AND DATA REDUCTION

The observations for all RGB stars in NGC 288 were taken on 2011 September 9–11 at the Cerro Tololo Inter-American Observatory (CTIO) using the Hydra multifiber spectrograph on the Blanco 4m telescope. Targets were selected from the RAdial Velocity Experiment (RAVE) database (Siebert et al. 2011), and only stars with radial velocities within $\pm 10 \text{ km s}^{-1}$ of the -46.4 km s^{-1} cluster velocity (Dinescu et al. 1999) were considered potential members. Cluster membership was also confirmed using *fxcor* in IRAF². Our derived radial velocities for NGC 288 stars are in agreement with the RAVE values. We find an average heliocentric radial velocity of -43.5 km s^{-1} ($\sigma=4.1 \text{ km s}^{-1}$), with individual values listed in Table 1.

Coordinates and photometry for potential members were taken from Lane et al. (2011) and 2MASS (Skrutskie et al. 2006). We utilized two different Hydra configurations to obtain spectra for ~ 50 RGB stars with luminosities ranging from the level of the horizontal branch to the RGB-tip. Color-magnitude diagrams illustrating the evolutionary state of all target stars are provided in Figure 1. Unfortunately, we were not able to fine-tune a configuration to obtain an equal number of stars on both the “blue” and “red” RGBs shown in the right panel of Figure 1. A single bench spectrograph setup was used for all observations. The setup included the use of the large ($300 \mu\text{m}$) fibers, 316 lines mm^{-1} Echelle grating, 400 mm Bench Schmidt camera, and E6257 filter to achieve a resolving power of $R(\lambda/\Delta\lambda \approx 18,000)$. The spectra ranged from $\sim 6145\text{--}6350 \text{ Å}$.

Basic data reduction was accomplished using the IRAF tasks *ccdproc* and *dohydra* to trim the overscan region, bias subtract the images, identify and trace the fibers, correct for scattered light, remove cosmic rays, apply the flat-field correction, linearize the wavelength scale based on ThAr lamp exposures, and to subtract the sky spectra. Telluric removal was carried out using the *telluric* IRAF task and observations of several rapidly-rotating B stars observed at various air masses. The reduced images were then corrected for heliocentric

²IRAF is distributed by the National Optical Astronomy Observatory, which is operated by the Association of Universities for Research in Astronomy, Inc., under cooperative agreement with the National Science Foundation.

velocity variations and co-added with the *scombine* task. Unfortunately, the observing conditions during all NGC 288 observations were poor and included light clouds and seeing of $\sim 1.5''$. This severely reduced the signal-to-noise ratios (S/N) of the spectra, leaving only 27 stars for which some abundances could be measured. The final co-added spectra had typical S/N of about 30.

3. ANALYSIS

3.1. Model Stellar Atmospheres

We utilized published photometry in the near-infrared J, H, and K_S bands from 2MASS to obtain effective temperatures (T_{eff}) with the color-temperature relation described in Alonso et al. (1999; 2001). In order to use the Alonso et al. (1999; 2001) calibration, we converted the dereddened 2MASS J–K_S colors onto the Telescopio Carlos Sánchez (TCS) system using the transformations summarized in Johnson et al. (2005). We assumed $E(B-V)=0.03$ (Harris 1996; 2010 edition) for the color excess and $E(J-K_S)/E(B-V)=0.527$ (Rieke & Lebofsky 1985). Surface gravity was determined using the standard relation,

$$\log(g_*) = 0.40(M_{\text{bol.}} - M_{\text{bol.}\odot}) + \log(g_\odot) + 4(\log(T/T_\odot)) + \log(M/M_\odot), \quad (1)$$

with the bolometric magnitude calculated from Buzzoni et al. (2010) and assuming a mass of $0.8 M_\odot$. Temperatures for the program stars ranged from 4185 to 5215 K and the surface gravity ranged from 0.95 to 2.30 cgs.

Individual model stellar atmospheres were created by interpolating within the α -enhanced (AODFNEW) ATLAS9 grid (Castelli et al. 1997). Temperatures and gravities were held fixed at their photometric values, and initial estimates for metallicity and microturbulence (v_t) were set at $[\text{Fe}/\text{H}]=-1.3$ and 2 km s^{-1} , respectively. Microturbulence was further refined by removing trends in Fe I abundance as a function of line strength. The final model metallicity was set as the average $[\text{Fe}/\text{H}]$ value derived from the Fe I lines. Our adopted model atmosphere parameters, along with available photometry, star identifications, and radial velocities, are provided in Table 1.

3.2. Derivation of Iron, Sodium, and Oxygen Abundances

Iron abundances were determined by measuring equivalent widths (EWs) for up to 25 Fe I lines, using the line list from Johnson et al. (2014, submitted). The EWs were measured using the fitting code developed for Johnson et al. (2008), which fits either a single Gaussian

or can deblend up to five nearby Gaussian profiles. The abundances were determined using the 2010 version of the LTE line analysis code MOOG (Snedden 1973). A summary of the average $[\text{Fe}/\text{H}]$ abundances is provided in Table 1.

For the measurement of sodium and oxygen abundances, we utilized the spectrum synthesis driver in MOOG and created synthetic spectra for each star in the wavelength regions 6150–6165 Å for Na and 6295–6305 Å for oxygen. The abundances of the other elements for each star were held constant, except the nitrogen abundance was used as a proxy to fit CN lines. We adopted the O and Na line lists from Johnson et al. (2014, submitted). The final abundances were set by fitting the smoothed synthetic spectrum to the observed spectrum by eye. Typical fitting uncertainties are ~ 0.10 dex. The $[\text{O}/\text{Fe}]$ and $[\text{Na}/\text{Fe}]$ ratios are provided in Table 1.

3.3. Abundance Uncertainties

In order to estimate the sensitivity of our derived abundances ratios due to uncertainties in the adopted model atmosphere parameters, we rederived the $[\text{Fe}/\text{H}]$, $[\text{O}/\text{Fe}]$, and $[\text{Na}/\text{Fe}]$ ratios by varying one parameter at a time and holding the others fixed. We estimated conservative uncertainties of $T_{\text{eff}} \pm 100$ K, $\log(g) \pm 0.3$ cgs, $[\text{M}/\text{H}] \pm 0.3$ dex, and $v_t \pm 0.15$ km s $^{-1}$. The average total uncertainty for $[\text{Fe}/\text{H}]$, $[\text{O}/\text{Fe}]$, and $[\text{Na}/\text{Fe}]$ is calculated to be ± 0.15 , ± 0.18 , and ± 0.16 dex, respectively. Since our iron and sodium abundances are based solely on the measurement of neutral lines, the derived $[\text{Fe}/\text{H}]$ and $[\text{Na}/\text{Fe}]$ values were most sensitive to variations in effective temperature. In contrast, the $[\text{O}/\text{Fe}]$ ratios, especially in the absence of reliable Fe II measurements, were most sensitive to uncertainties in the surface gravity. Individual errors, taking into account the line-to-line abundance dispersion and all model parameter uncertainties, are listed in Table 1.

4. RESULTS AND DISCUSSION

4.1. Basic Composition Results

Previous large sample ($\gtrsim 10$ stars), high resolution spectroscopic analyses of NGC 288 have found the cluster to be moderately metal-poor, with estimates ranging from $\langle [\text{Fe}/\text{H}] \rangle = -1.22$ ($\sigma = 0.04$; Carretta et al. 2009a) to $\langle [\text{Fe}/\text{H}] \rangle = -1.39$ ($\sigma = 0.04$; Shetrone & Keane 2000). We find in agreement with past work that NGC 288 has $\langle [\text{Fe}/\text{H}] \rangle = -1.19$ ($\sigma = 0.12$). Although the star-to-star dispersion in $[\text{Fe}/\text{H}]$ is larger than those reported in previous studies (e.g., Carretta et al. 2009a), this is likely due to the moderate S/N of our data and does not

signify the existence of an intrinsic metallicity spread within the cluster.

The O–Na anti–correlation and CN/CH variations, which are common features of nearly all Galactic globular clusters (e.g., Gratton et al. 2004; 2012), has been previously reported in NGC 288 stars (e.g., Shetrone & Keane 2000; Kayser et al. 2008; Carretta et al. 2009a; 2009b; Smith & Langland–Shula 2009). The light element abundance variations in NGC 288 have also been linked to two populations having slightly different He abundances ($\Delta Y=0.013$; Piotto et al. 2013). While we cannot directly test for He abundance variations with our current data set, we have measured $[\text{O}/\text{Fe}]$ (20/27 stars) and $[\text{Na}/\text{Fe}]$ (26/27 stars) abundances. As can be seen in Figure 2, we confirm the existence of the O–Na anti–correlation in NGC 288. We also find $\langle [\text{O}/\text{Fe}] \rangle = +0.25$ ($\sigma=0.13$) and $\langle [\text{Na}/\text{Fe}] \rangle = +0.15$ ($\sigma=0.26$), which is in reasonable agreement with past work by Carretta et al. (2009a; $\langle [\text{O}/\text{Fe}] \rangle = +0.11$; $\sigma=0.26$; $\langle [\text{Na}/\text{Fe}] \rangle = +0.27$; $\sigma=0.26$) and Shetrone & Keane (2000; $\langle [\text{O}/\text{Fe}] \rangle = +0.22$; $\sigma=0.14$; $\langle [\text{Na}/\text{Fe}] \rangle = +0.20$; $\sigma=0.25$).

Previous work on the CN and CH variations of sub–giant branch stars (e.g., Kayser et al. 2008; Smith & Langland–Shula 2009), as well as the O, Na, and Al abundances in RGB stars (e.g., Shetrone & Keane 2008; Carretta et al. 2009a; 2009b), found some indications that the light element chemistry may be distributed in a bimodal manner. While the $[\text{O}/\text{Fe}]$ and $[\text{Na}/\text{Fe}]$ data presented here do not exhibit a strongly bimodal distribution, possibly because of the lower S/N of our spectra and modest sample size, such a distribution may provide an important clue in understanding the split RGB reported in Roh et al. (2011).

4.2. A New CTIO Ca Filter Tracing and Linking the Split RGB to Chemical Composition

Although Roh et al. (2011) initially ruled out contamination of the CTIO Ca filter from the CN band at $\sim 3885 \text{ \AA}$, based on previous filter tracing data, the authors noted that the colors of the split RGB in NGC 288 were correlated with the cyanogen index measurements of Kayser et al. (2008). In particular, they found that the “CN–normal” (i.e., halo–like composition) stars were located on the blue RGB but the “CN–strong” stars were located on the red RGB (see Figure 4 of Roh et al. 2011). If real, the chemical distinction between the two branches should also be detectable on the upper RGB as differences in $[\text{O}/\text{Fe}]$ and $[\text{Na}/\text{Fe}]$ abundances because CN–normal and CN–strong stars are expected to be O–rich/Na–poor and O–poor/Na–rich, respectively.

In Figure 2 we investigated the correlation between RGB color and light element abundances, using both our data and those from Carretta et al. (2009a), and found the same

correlation between color and composition. While the dispersion in both $[\text{O}/\text{Fe}]$ and $[\text{Na}/\text{Fe}]$ is roughly a factor of two in magnitude, the blue RGB is clearly dominated by stars with higher $[\text{O}/\text{Fe}]$ and lower $[\text{Na}/\text{Fe}]$ compared to the red RGB. On average, the blue RGB stars from the combined data set have $\langle[\text{O}/\text{Fe}]\rangle=+0.27$ ($\sigma=0.19$) and $\langle[\text{Na}/\text{Fe}]\rangle=+0.11$ ($\sigma=0.16$) while the red RGB stars have $\langle[\text{O}/\text{Fe}]\rangle=+0.08$ ($\sigma=0.24$) and $\langle[\text{Na}/\text{Fe}]\rangle=+0.43$ ($\sigma=0.19$). In contrast, the difference in $[\text{Fe}/\text{H}]$ between the two branches is mostly negligible, with the blue RGB having $\langle[\text{Fe}/\text{H}]\rangle=-1.19$ ($\sigma=0.08$) and the red RGB having $\langle[\text{Fe}/\text{H}]\rangle=-1.24$ ($\sigma=0.06$). Therefore, we conclude that the split RGB in NGC 288 is driven almost exclusively by differences in light element composition (and possibly He) rather than a difference of 0.16 dex in $[\text{M}/\text{H}]$ and 1.5 Gyr in age, as suggested by Roh et al. (2011).

The remaining question is *why* the data from Roh et al. (2011) show a double RGB when the CTIO Ca filter is supposed to avoid major contamination from nearby molecular CN bands. To investigate this further, we requested a new transmission curve of the CTIO Ca narrow-band filter. The filter response was measured using a Cary 500 spectrophotometer at Gemini Observatory with a collimated beam at incident angle. The new filter response curve (A. Kunder & D. Hölk 2012, private communication) is shown in Figure 3 (see also Table 2), along with the original data provided to Roh et al. (2011). It is clear from Figure 3 that the CTIO Ca filter actually peaks in transmissivity near 3900 Å, and thus can be significantly contaminated by the CN band blueward of ~ 3885 Å in cool stars. As mentioned in Lee et al. (2009) and Roh et al. (2011), the CN contamination is likely to be increased when the filter is placed at prime focus and the peak transmission shifts blueward. This is the root cause of the split RGB found by Roh et al. (2011). A new filter, specifically designed to trace only the Ca HK region without significant CN contamination and used with the du Pont 2.5m at Las Campanas Observatory, confirms our result as the double RGB in NGC 288 disappears in updated y vs hk color-magnitude diagrams (Lee et al. 2014, in prep.; see also Lee et al 2013). Interestingly, although the CTIO Ca filter may be too contaminated to use with the Ca HK lines, it may be an efficient filter for separating CN-normal and CN-strong stars in other stellar populations.

In addition to NGC 288, the CN contamination also likely explains the RGB hk index spreads in the other clusters (NGC 2808, M4, M5, NGC 6752, and NGC 6397) observed by Lee et al. (2009) for which significant $[\text{Ca}/\text{H}]$ and/or $[\text{Fe}/\text{H}]$ variations are not confirmed by high-resolution spectroscopy (e.g., Carretta et al. 2010). However, the RGB hk index spreads are likely real in the remaining clusters ω Cen, M22, and NGC 1851 (e.g., Lee et al. 2009; Joo & Lee 2013), which have spectroscopically confirmed star-to-star $[\text{Ca}/\text{H}]$ and/or $[\text{Fe}/\text{H}]$ variations. Finally, we note that while Yong et al. (2013) find a statistically significant correlation between Na and Ca abundances in NGC 6752, the amplitudes of the star-to-star abundance variations are at the few percent level. This effect, if also present in

a similarly monometallic cluster such as NGC 288, is likely not strong enough to contribute significantly to the broadly separated color sequences seen in the Roh et al. (2011) y vs hk color–magnitude diagrams.

5. SUMMARY

We derived $[\text{Fe}/\text{H}]$, $[\text{O}/\text{Fe}]$, and $[\text{Na}/\text{Fe}]$ abundances for 27 RGB stars in the Galactic globular cluster NGC 288 using high resolution spectra obtained with the Hydra multifiber spectrograph on the Blanco 4m telescope at CTIO. We find that the cluster has a negligible spread in metallicity with an average $[\text{Fe}/\text{H}]=-1.19$ ($\sigma=0.12$). We also confirm the existence of the O–Na anti–correlation in NGC 288 RGB stars. The average oxygen and sodium abundances from our sample are $\langle[\text{O}/\text{Fe}]\rangle=+0.25$ ($\sigma=0.13$) and $\langle[\text{Na}/\text{Fe}]\rangle=+0.15$ ($\sigma=0.26$), respectively. Furthermore, we find that the two giant branches previously noted by Roh et al. (2011) are driven by differences in the abundances of elements from carbon through sodium (and probably also magnesium and aluminum), rather than a combination of age and metallicity spreads. In general, the blue RGB stars have significantly higher $[\text{O}/\text{Fe}]$ and lower $[\text{Na}/\text{Fe}]$ than the red RGB stars. Further investigation of the double RGB lead us to discover that this feature was due primarily to contamination by a CN–band blueward of 3885 Å in the original data set. A new filter response curve, obtained for this study, revealed the peak transmission to be >50 Å bluer than originally thought, and is thus the real cause of the double RGB found in Roh et al. (2011).

We thank the referee for a careful review and thoughtful comments that lead to an improvement of the manuscript. This publication makes use of data products from the Two Micron All Sky Survey, which is a joint project of the University of Massachusetts and the Infrared Processing and Analysis Center/California Institute of Technology, funded by the National Aeronautics and Space Administration and the National Science Foundation. We thank the Cerro Tololo Inter–American Observatory (CTIO) staff Daniel Hölck and Andrea Kunder for providing the new response curve for the CTIO Ca filter. CIJ gratefully acknowledges support from the Clay Fellowship, administered by the Smithsonian Astrophysical Observatory. This material is based upon work supported by the National Science Foundation under award No. AST–1003201 to CIJ. RMR acknowledges support from NSF grants AST–0709479 and AST–12112099. Y.–W. L. acknowledges support from NRF of Korea to CGER.

REFERENCES

- Alonso, A., Arribas, S., & Martínez-Roger, C. 1999, *A&AS*, 140, 261
- Alonso, A., Arribas, S., & Martínez-Roger, C. 2001, *A&A*, 376, 1039
- Buzzoni, A., Patelli, L., Bellazzini, M., Pecci, F. F., & Oliva, E. 2010, *MNRAS*, 403, 1592
- Carretta, E., Bragaglia, A., Gratton, R. G., et al. 2009a, *A&A*, 505, 117
- Carretta, E., Bragaglia, A., Gratton, R., & Lucatello, S. 2009b, *A&A*, 505, 139
- Carretta, E., Bragaglia, A., Gratton, R., et al. 2010, *ApJ*, 712, L21
- Castelli, F., Gratton, R. G., & Kurucz, R. L. 1997, *A&A*, 318, 841
- D’Ercole, A., Vesperini, E., D’Antona, F., McMillan, S. L. W., & Recchi, S. 2008, *MNRAS*, 391, 825
- de Mink, S. E., Pols, O. R., Langer, N., & Izzard, R. G. 2009, *A&A*, 507, L1
- Decressin, T., Meynet, G., Charbonnel, C., Prantzos, N., & Ekström, S. 2007, *A&A*, 464, 1029
- Denissenkov, P. A., & Hartwick, F. D. A. 2014, *MNRAS*, 437, L21
- Dinescu, D. I., Girard, T. M., & van Altena, W. F. 1999, *AJ*, 117, 1792
- Gratton, R., Sneden, C., & Carretta, E. 2004, *ARA&A*, 42, 385
- Gratton, R. G., Carretta, E., & Bragaglia, A. 2012, *A&A Rev.*, 20, 50
- Harris, W. E. 1996, *AJ*, 112, 1487
- Izzard, R. G., de Mink, S. E., Pols, O. R., et al. 2013, *Mem. Soc. Astron. Italiana*, 84, 171
- Johnson, C. I., Kraft, R. P., Pilachowski, C. A., et al. 2005, *PASP*, 117, 1308
- Johnson, C. I., Pilachowski, C. A., Simmerer, J., & Schwenk, D. 2008, *ApJ*, 681, 1505
- Joo, S.-J., & Lee, Y.-W. 2013, *ApJ*, 762, 36
- Karakas, A. I. 2010, *MNRAS*, 403, 1413
- Kayser, A., Hilker, M., Grebel, E. K., & Willemsen, P. G. 2008, *A&A*, 486, 437
- Lane, R. R., Kiss, L. L., Lewis, G. F., et al. 2011, *A&A*, 530, A31

- Lee, J.-W., Kang, Y.-W., Lee, J., & Lee, Y.-W. 2009, *Nature*, 462, 480
- Lee, Y.-W., Han, S.-I., Joo, S.-J., et al. 2013, *ApJ*, 778, L13
- Monelli, M., Milone, A. P., Stetson, P. B., et al. 2013, *MNRAS*, 431, 2126
- Piotto, G. 2009, *IAU Symposium*, 258, 233
- Piotto, G., Milone, A. P., Marino, A. F., et al. 2013, *ApJ*, 775, 15
- Rieke, G. H., & Lebofsky, M. J. 1985, *ApJ*, 288, 618
- Roh, D.-G., Lee, Y.-W., Joo, S.-J., et al. 2011, *ApJ*, 733, L45
- Shetrone, M. D., & Keane, M. J. 2000, *AJ*, 119, 840
- Siebert, A., Williams, M. E. K., Siviero, A., et al. 2011, *AJ*, 141, 187
- Skrutskie, M. F., Cutri, R. M., Stiening, R., et al. 2006, *AJ*, 131, 1163
- Smith, G. H., & Langland-Shula, L. E. 2009, *PASP*, 121, 1054
- Snedden, C. 1973, *ApJ*, 184, 839
- Valcarce, A. A. R., & Catelan, M. 2011, *A&A*, 533, A120
- Ventura, P., & D’Antona, F. 2008, *MNRAS*, 385, 2034
- Yong, D., Meléndez, J., Grundahl, F., et al. 2013, *MNRAS*, 434, 3542

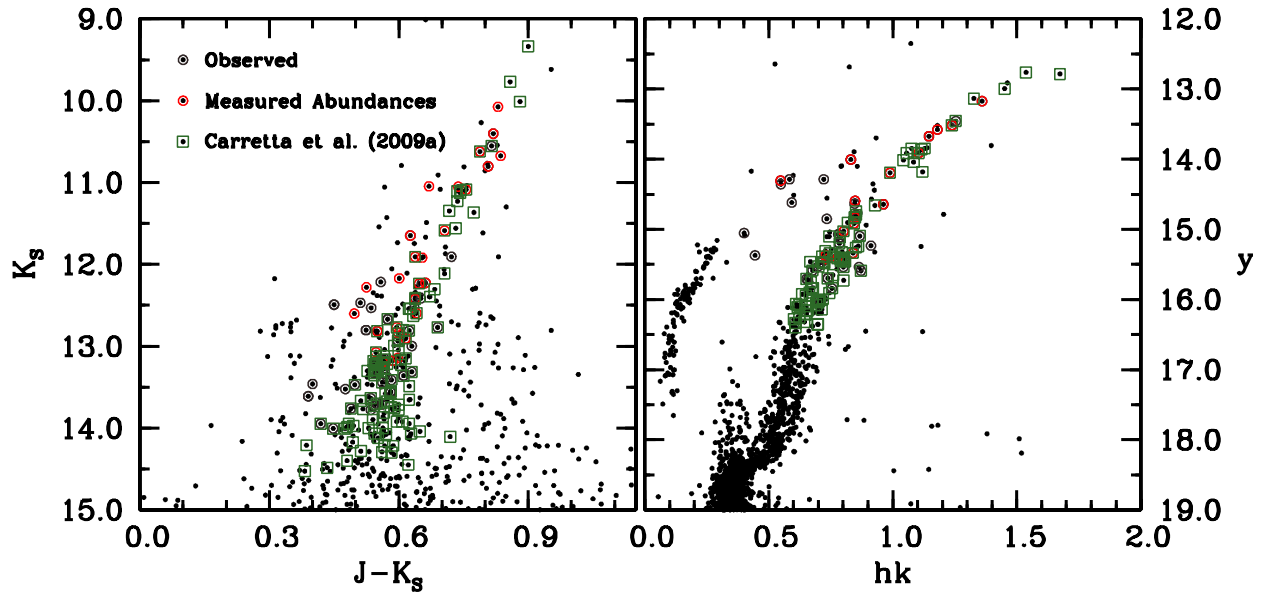


Fig. 1.— *left*: A 2MASS K_s versus $J-K_s$ color-magnitude diagram illustrating the targets observed in the present work (open grey circles), those for which the S/N was high enough to derive abundance ratios (open red circles), and those observed in Carretta et al. (2009a; open green boxes). *right*: A similar color-magnitude diagram using the hk and y -band photometric data from Roh et al. (2011). Note the double RGB.

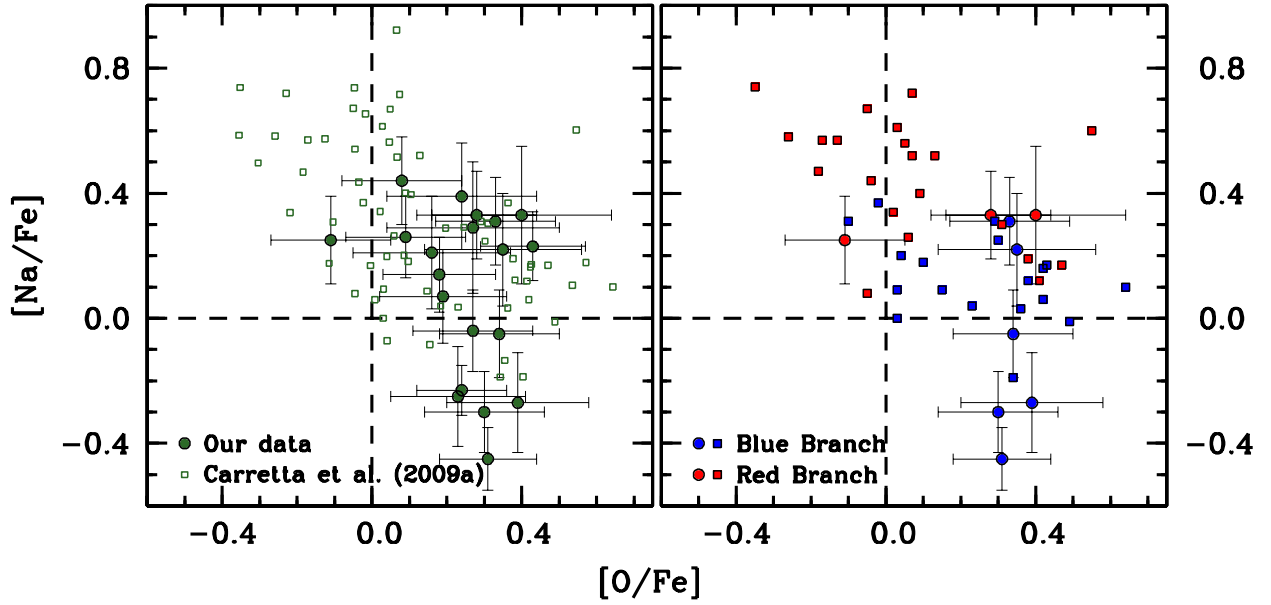


Fig. 2.— *left*: A plot of $[Na/Fe]$ versus $[O/Fe]$ for stars in the present work (filled green circles) and Carretta et al. (2009a; open green boxes). *right*: A similar plot showing the O–Na anti-correlation in the present data (circles) and Carretta et al. (2009a; boxes), but the stars are color-coded depending on whether each lies on the blue or red RGB in Figure 1. Horizontal branch, AGB, and RGB-tip stars that cannot be reliably assigned to either RGB in Figure 1 have been omitted in this panel. The red RGB stars have predominantly low $[O/Fe]$ and high $[Na/Fe]$ ratios. In contrast, the blue RGB stars typically have comparatively high $[O/Fe]$ and low $[Na/Fe]$ ratios.

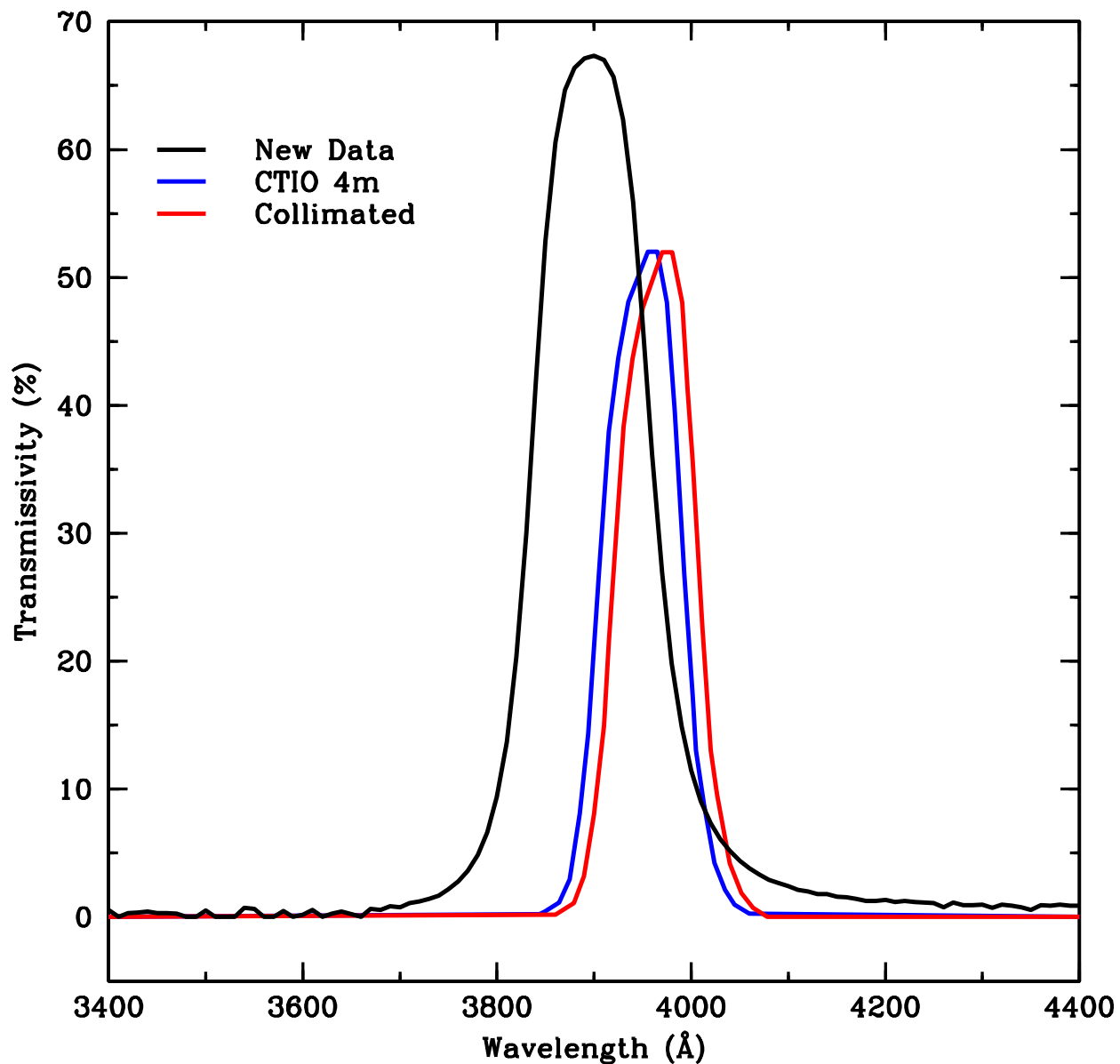


Fig. 3.— The old filter response curve for the CTIO Ca filter, including for both a collimated beam (red line) and mounted at prime focus (blue line), are compared with the newly measured filter response function (black line). Note in particular that the new lab measurement finds the peak transmissivity to occur near 3900 Å, which is >50 Å bluer than the original curve. When compared with Figure 4 in Roh et al. (2011), it is clear that the CTIO Ca filter is contaminated by the CN-band blueward of ~ 3885 Å.

Table 1. Star Identifications, Coordinates, Model Atmosphere Parameters, and Radial Velocities

ID 2MASS	RA (J2000) (degrees)	DEC (J2000) (degrees)	J (mag.)	H (mag.)	K _S (mag.)	T _{eff} (K)	log(g) (cgs)	[Fe/H]	vt (km s ⁻¹)	[O/Fe]	[Na/Fe]	[Fe/H] Error	[O/Fe] Error	[Na/Fe] Error	RV _{helio.} (km s ⁻¹)
00521548–2641039	13.064524	–26.684423	13.366	12.815	12.816	5015	2.15	–0.94	1.60	...	+0.54	0.14	...	0.15	–42.1
00522151–2632418	13.089655	–26.544960	11.221	10.578	10.402	4225	1.05	–1.13	1.70	+0.23	–0.25	0.15	0.18	0.16	–43.8
00523129–2639008	13.130410	–26.650232	13.098	12.693	12.601	5215	2.10	–1.23	2.00	+0.43	+0.23	0.10	0.14	0.11	–39.7
00523149–2636016	13.131247	–26.600452	12.881	12.320	12.234	4690	1.85	–1.19	1.40	+0.24	+0.39	0.17	0.20	0.17	–38.8
00523688–2630586	13.153706	–26.516281	12.572	11.985	11.918	4665	1.75	–1.01	1.60	+0.16	+0.21	0.18	0.21	0.18	–41.9
00523795–2636064	13.158162	–26.601801	13.062	12.560	12.424	4715	1.95	–1.04	1.30	+0.39	–0.27	0.16	0.19	0.16	–41.1
00523890–2635317	13.162090	–26.592154	11.609	10.923	10.802	4255	1.25	–1.23	1.50	+0.30	–0.30	0.12	0.16	0.13	–46.1
00523998–2633498	13.166596	–26.563854	11.842	11.195	11.086	4380	1.35	–1.09	1.50	+0.24	–0.23	0.07	0.12	0.08	–42.2
00524033–2636328	13.168067	–26.609137	13.621	13.112	13.074	5025	2.25	–1.13	2.00	+0.40	+0.33	0.22	0.24	0.22	–45.4
00524057–2628033	13.169044	–26.467602	13.438	12.901	12.839	4840	2.10	–1.29	1.90	+0.09	+0.26	0.12	0.16	0.13	–41.7
00524095–2634390	13.170638	–26.577507	12.771	12.248	12.170	4835	1.85	–1.01	1.45	+0.34	–0.05	0.13	0.16	0.14	–41.0
00524379–2638018	13.182459	–26.633837	11.715	11.151	11.045	4620	1.40	–1.32	1.80	+0.19	+0.07	0.14	0.17	0.15	–41.8
00524526–2633297	13.188614	–26.558271	12.805	12.381	12.280	5105	1.95	–1.36	2.00	...	+0.41	0.22	...	0.22	–42.0
00524625–2635494	13.192748	–26.597057	11.410	10.729	10.622	4300	1.15	–1.33	1.75	+0.28	+0.33	0.13	0.16	0.14	–39.3
00524655–2631523	13.193994	–26.531214	13.520	12.940	12.904	4785	2.15	–1.24	1.80	...	+0.09	0.29	...	0.29	–42.0
00524910–2640072	13.204609	–26.668690	13.237	12.661	12.596	4705	2.00	–1.21	1.40	+0.33	+0.31	0.13	0.16	0.14	–44.1
00524957–2642106	13.206557	–26.702971	11.788	11.176	11.050	4430	1.35	–1.17	1.65	+0.27	–0.04	0.12	0.16	0.13	–48.7
00524958–2637006	13.206591	–26.616846	13.741	13.235	13.143	4845	2.25	–1.26	1.55	...	+0.21	0.11	...	0.12	–42.7
00524977–2635118	13.207381	–26.586620	12.546	11.970	11.908	4715	1.75	–1.29	1.75	+0.08	+0.44	0.13	0.16	0.14	–42.2
00524981–2636559	13.207542	–26.615547	12.293	11.675	11.587	4515	1.60	–1.41	1.75	...	+0.41	0.20	...	0.20	–49.4
00525240–2632252	13.218359	–26.540346	13.758	13.285	13.195	4965	2.30	–1.20	1.95	...	+0.30	0.15	...	0.16	–42.0
00525279–2634388	13.219980	–26.577454	11.510	10.798	10.674	4185	1.20	–1.11	1.50	+0.31	–0.45	0.09	0.13	0.10	–52.2
00525287–2635201	13.220298	–26.588942	10.905	10.197	10.075	4200	0.95	–1.32	2.00	+0.27	+0.29	0.21	0.23	0.21	–56.2
00525460–2637084	13.227506	–26.619019	12.275	11.780	11.648	4750	1.65	–1.30	1.90	+0.18	+0.14	0.11	0.15	0.12	–45.4
00525842–2637498	13.243453	–26.630505	13.762	13.185	13.176	4885	2.25	–1.05	1.35	+0.35	+0.22	0.18	0.21	0.18	–38.7
00531301–2637047	13.304216	–26.617979	12.888	12.305	12.226	4645	1.85	–1.20	1.80	–0.11	+0.25	0.13	0.16	0.14	–43.0
00531493–2633524	13.312218	–26.564575	13.363	12.820	12.768	4855	2.10	–1.20	1.65	0.21	–41.5

Table 2. CTIO Ca Filter Response

Wavelength (Å)	Transmission (%)
3400	0.55
3410	0.00
3420	0.30
3430	0.36
3440	0.42
3450	0.30
3460	0.30
3470	0.25
3480	0.00
3490	0.00
3500	0.51
3510	0.00
3520	0.00
3530	0.00
3540	0.72
3550	0.65
3560	0.00
3570	0.00
3580	0.46
3590	0.00
3600	0.20
3610	0.55
3620	0.00
3630	0.25
3640	0.42
3650	0.22
3660	0.00
3670	0.62
3680	0.57
3690	0.83

Table 2—Continued

Wavelength (Å)	Transmission (%)
3700	0.76
3710	1.10
3720	1.22
3730	1.42
3740	1.69
3750	2.16
3760	2.80
3770	3.60
3780	4.84
3790	6.63
3800	9.38
3810	13.68
3820	20.32
3830	30.04
3840	41.90
3850	52.84
3860	60.57
3870	64.63
3880	66.39
3890	67.13
3900	67.34
3910	67.00
3920	65.67
3930	62.35
3940	55.92
3950	46.48
3960	36.17
3970	26.90
3980	19.86
3990	14.90

Table 2—Continued

Wavelength (Å)	Transmission (%)
4000	11.44
4010	9.07
4020	7.35
4030	6.10
4040	5.17
4050	4.39
4060	3.81
4070	3.31
4080	2.91
4090	2.68
4100	2.42
4110	2.14
4120	2.01
4130	1.80
4140	1.79
4150	1.61
4160	1.53
4170	1.42
4180	1.28
4190	1.27
4200	1.33
4210	1.19
4220	1.26
4230	1.17
4240	1.15
4250	1.10
4260	0.78
4270	1.13
4280	0.94
4290	0.95

Table 2—Continued

Wavelength (Å)	Transmission (%)
4300	0.97
4310	0.73
4320	0.97
4330	0.88
4340	0.74
4350	0.54
4360	0.94
4370	0.88
4380	0.96
4390	0.87
4400	0.91